Friction **11**(2): 259–279 (2023)
https://doi.org/10.1007/s40544-022-0599-4
ISSN 2223-7690
CN 10-1237/TH
RESEARCH ARTICLE

Dry friction damping mechanism of flexible microporous metal rubber based on cell group energy dissipation mechanism

Liangliang SHEN[1,2], Zhiying REN[1,2,*], Jian XU[3,*], Lin PAN[1,4], Youxi LIN[1,4], Hongbai BAI[1,2]

[1] *School of Mechanical Engineering and Automation, Fuzhou University, Fuzhou 350116, China*

[2] *Engineering Research Center for Metal Rubber, Fuzhou University, Fuzhou 350116, China*

[3] *State Key Laboratory of Fine Chemicals, Liaoning High Performance Polymer Engineering Research Center, School of Chemical Engineering, Dalian University of Technology, Dalian 116024, China*

[4] *Fuzhou Friction and Lubrication Industry Technology Innovation Center, Fuzhou 350108, China*

Received: 17 October 2021 / Revised: 20 November 2021 / Accepted: 08 January 2022

Abstract: Flexible microporous metal rubber (FMP-MR) is a high-damping material that dissipates energy by dry friction through internal spiral metal wires in contact with each other. However, the FMP-MR energy dissipation mechanism is not fully understood owing to its disordered grid interpenetrating structure. In this work, computer-aided preparation technology is used to accurately reconstruct the complex spiral network structure of FMP-MR multipoint random contact, and a cell group model with an energy dissipation mechanism is proposed to obtain the dynamic energy distribution of the contact friction in both space and time dimensions. By judging the effective contact point, a global displacement ablation phenomenon of hooked staggered porous materials is induced. The macro- and micro-equivalent frictions are introduced to effectively explain the characteristics of the strong energy dissipation in FMP-MR under fretting excitation. A real and effective damping hysteresis constitutive model is then constructed to dynamically capture the mapping relationship between the complex nonlinear topological structure effect of the materials and spatial random contact dry friction in real time. The results indicate that the contact behavior between turns of the FMP-MR wire follows a clear quasi-Gaussian distribution under an external load, forcing the topological results to change. The energy dissipation of the materials revealed peak energy consumption lagging behind the loading limit for a certain distance, which can be determined by the effective contact point and contact dry friction slip. The consistency between the quasi-static compression tests and constitutive curves of the model was quantitatively verified through residual analysis. The data demonstrated the differential behavior of the FMP-MR meso-structure to follow a phased growth law during loading with different action mechanisms in the guiding, main growth, and relaxation stages of the energy consumption displacement curve. In summary, these findings provide an acceptable theoretical basis for the damping energy consumption mechanism and lifetime prediction of FMP-MR.

Keywords: flexible microporous metal rubber (FMP-MR); effective contact; energy dissipation; dry friction; damping hysteresis

1 Introduction

Flexible microporous metal rubber (FMP-MR) is a damping material with a complex spiral network structure. FMP-MR is mainly made of stainless steel [1, 2], copper alloy [3], shape memory alloy [4, 5], or other metal materials assembled by winding, stretching, and other pretreatment stages to form metal wire

*Corresponding authors: Zhiying REN, E-mail: renzy@fzu.edu.cn; Jian XU, E-mail: xujian@nimte.ac.cn

spiral coils with a certain pitch. Subsequently, the spiral coils are wound on a cylindrical mandrel surface at a specific angle θ to yield an FMP-MR blank with interlocking and hooking characteristics. As displayed in Fig. 1, a blank placed in a specific die is stamped and formed by FMP-MR during the specific preparation process. Compared to traditional polymer rubber materials, FMP-MR not only demonstrates excellent vibration reduction characteristics but also meets the special environmental requirements of high/low temperature [6, 7], high pressure, strong corrosion [8], and severe vibration [9], and features suitable for use in aerospace [10, 11], deep-sea strike [12–14], and medical equipment [15].

FMP-MR is a porous elastic material with a unique damping hysteresis and energy-absorption mechanism. As indicated in Fig. 2(b), the inner turns of FMP-MR reveal mutual folding, extrusion, and dry friction slippage under an external load. In addition, the space between the FMP-MR turns becomes smaller under loading, and the density of meso-turns become significant. At the macro-scale, FMP-MR demonstrates a certain short-term dimensional shrinkage in the loading direction. At the meso-scale, the majority of kinetic energy is dissipated in the form of dry friction slip based on heat loss, except for the elastic potential energy stored in the inner coil by self-compression due to the absorption of external kinetic energy. As the wire turn density increases in the material structure, the growing dry friction behavior breaks its quasi-linear mechanical equilibrium condition. In this case, the mechanical curve reflects, to a certain extent, an exponential growth trend as indicated in the exponential growth stage in Fig. 2(c). After the gradual unloading of the external load, the material undergoes a gradual rebound phenomenon at the

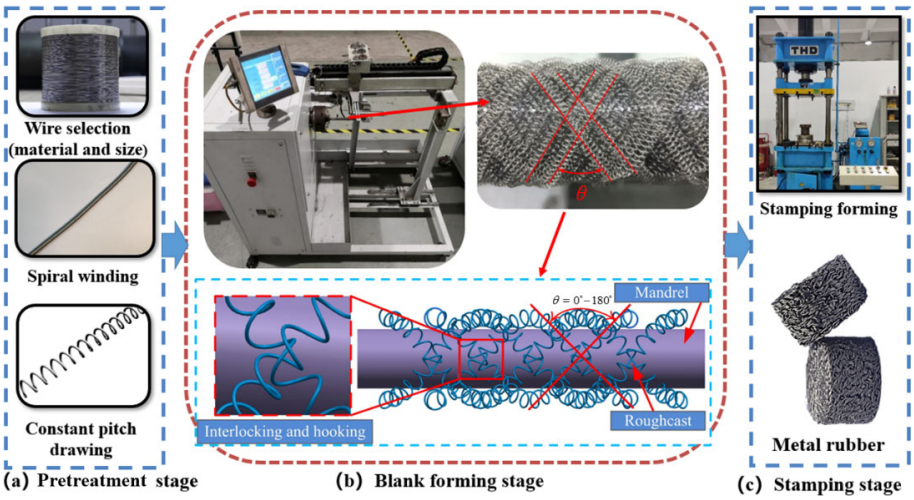

Fig. 1 Preparation flow chart of FMP-MR.

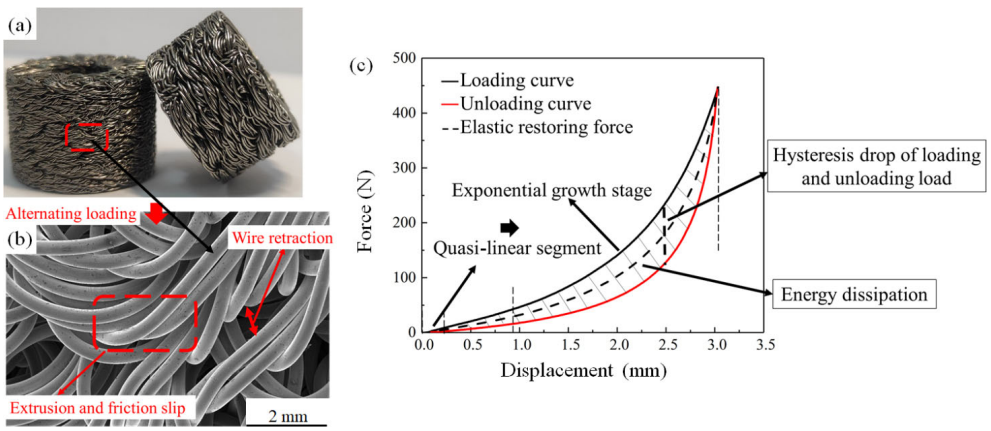

Fig. 2 Multiscale behavior of FMP-MR. (a) FMP-MR sample, (b) SEM meso-morphology, and (c) macroscopic hysteresis performance.

macro-scale until it reaches recovery owing to the self-elastic behavior of the FMP-MR inner spiral coil. The internal spiral coil of the FMP-MR releases part of the elastic potential energy stored in the excited environment. This induces secondary reverse contact dry friction between the turns and causes other energy loss in the form of dry friction. Therefore, the macro mechanical behavior of FMP-MR under the dual effects of loss in external energy and potential energy loss effect can lead to less unloading force presented by the hysteresis loop than the loading force.

Numerous studies have been devoted to the hysteresis theory of FMP-MR damping. Ao et al. [16] used the Poisson distribution to characterize the contact form between wire turns inside FMP-MR, and combined the simulations with experiments to effectively identify the parameters in the material damping constitutive relationship. Li and Wang [17] performed in-depth research on the mathematical model of dry friction between two solid contact surfaces, namely the Coulomb friction, hysteresis, numerical calculation of dry friction in dynamic systems, and cubic nonlinear stick damping bilinear hysteresis models. They also analyzed the generation mechanism of FMP-MR dry friction damping materials from a microscopic point of view. This approach based on mathematical modeling reflected, to a certain extent, the FMP-MR damping hysteresis characteristics, but seriously deviated from the actual structure of the material. Wu et al. [18] considered the sensitivity of the preparation parameters and used the cantilever curved beam model to deeply explore the FMP-MR meso-damping hysteresis characteristics. Zou et al. [19] constructed a regular microelement model based on the characteristics of the wire turns in FMP-MR to deeply explore the dry friction phenomenon during the wire turn sliding contact. In addition, they obtained the FMP-MR dry friction damping force. Cao et al. [20, 21] analyzed the spatial configuration and contact mode of wire turns in materials based on anisotropic deformation in the FMP-MR forming/non-forming direction. Moreover, the authors established a damping hysteresis mechanical model in the FMP-MR forming/non-forming direction. However, the local FMP-MR structural characteristics considered through the combination of cantilever curved beams, microelements, and other models with single and regular distribution forms and dry friction theory remain unable to reflect the disordered distribution form of the wire turns in materials. In addition, finding an effective mapping relationship with macro preparation parameters remains a challenge.

Liu et al. [22] conducted dynamic damping experiments based on the dynamic performance of FMP-MR damping pads and analyzed the variation laws of the FMP-MR damping loss coefficient for different material parameters and load forms. They found the commonly used damping capacity test method based on linear material to be not applicable owing to the nonlinear characteristics of FMP-MR. Therefore, Hou et al. [23] proposed a damping capacity test method based on hysteretic curve decomposition to effectively characterize the FMP-MR damping properties. Gadot et al. [24] identified the unique adjustable super-elasticity and shape memory properties in FMP-MR based on a Ni–Ti alloy. Three-dimensional (3D) X-ray microtomography experiments demonstrated that FMP-MR based on this Ni–Ti material possessed the excellent shape memory recovery ability under the heating state at a strain of 16%. Ertas et al. [25] prepared the FMP-MR dampers braided with 304 stainless steel, nickel–chromium–iron-based solution strengthening alloy, copper, and nickel–titanium shape memory alloy. The effects of amplitude and frequency on the stiffness and damping coefficient were explored through steady-state forced vibration and transient vibration experiments. Yang et al. [26] combined material dynamics experiments to evaluate the vibration reliability by proposing the section distortion coefficient in addition to studying the vibration reliability and damping performance of annular FMP-MR under cyclic dynamic loads. Experimental research methods can be used to obtain the damping characteristics of FMP-MR under specific parameters. However, the unpredictability of the tests makes it difficult to deeply explore the dry friction behavior mechanism contained in such spatial micropore structure materials.

Overall, the above findings suggest extensive qualitative analysis from macro dynamic tests. However, these phenomena have been explained only through the phenomenological equivalent model by frequently ignoring the FMP-MR internal complex disordered structural characteristics. To date, only

limited studies related to the FMP-MR damping hysteresis characteristics from the perspective of dry friction energy consumption have been reported. Moreover, the contact, friction, and slip phenomena of wire turns under an external load have demonstrated a discrete dynamic form because FMP-MR is essentially a disordered discontinuous structural material; this makes it difficult to effectively display and quantitatively characterize.

In this work, hollow and solid cylinder FMP-MR commonly used in engineering as the research objects are selected to construct a finite element model close to a real FMP-MR structure through the spatial geometric coordinate iteration mechanism and secondary compilation method of finite elements. Combined with the cellular model, the spatial morphology of FMP-MR is accurately reconstructed in a time series. The effects of parameters such as the normal force, dynamic friction, and fretting displacement vector on the macroscopic energy dissipation are examined. To further reveal the energy dissipation mechanism and dry friction lifetime behavior of the material, multiscale mapping relationships among the macro process parameters, meso-turn structure, and FMP-MR dry friction damping energy dissipation capacity are studied based on the dry friction energy dissipation behavior of the internal meso-structure of the material.

2 Energy dissipation constitutive relationship based on FMP-MR multiscale dry friction damping

2.1 Finite element model of FMP-MR based on computer-aided technology (CAT) preparation method

CAT could possibly reflect the disordered wire turn interpenetration phenomena of FMP-MR and provide a powerful means for studying the meso-behavior mechanisms of materials. As indicated in Fig. 3, from the generation of a single spiral coil to the preparation of the initial blank, it maximally approaches the preparation process.

The common material of FMP-MR was composed of 304 austenitic stainless steel. The material parameters were set as the Young's modulus of 2.06×10^5 MPa, the density of 7.93×10^{-3} g/mm^3, and the Poisson's ratio of 0.3. The explicit power element BEAM161 was selected for meshing, which is a special element for solving explicit dynamics in ANSYS, and is suitable for the finite element analysis of complex multipoint contact. The Hughes–Liu cross-sectional integral was used for element calculation in addition to the integral rule of the order Gauss integral. The FMP-MR stamping forming, loading, and unloading processes were simulated by setting the piecewise plastic properties, tangent modulus, failure strain, and strain rate parameters. The details of the specific realization process can be found in Ref. [27]. In this work, hollow ring and solid cylinder FMP-MRs were used in engineering as research objects. To reduce the calculation cost, a 1/6 model was selected for the calculation and analysis. The specific preparation process parameters are summarized in Table 1, and the virtual stamping process is displayed in Fig. 4.

Under the certain pressure, the FMP-MR blank gradually realized the spatial contact judgment between the twisted coils and the elastic–plastic sliding extrusion process. After the elastic rebound phenomenon following the mold unloading, an FMP-MR finite element model with different shapes was constructed. To further illustrate the reliability of the FMP-MR finite element model based on computer-aided preparation technology, physical FMP-MR with the same parameters was prepared for comparison and verification. As

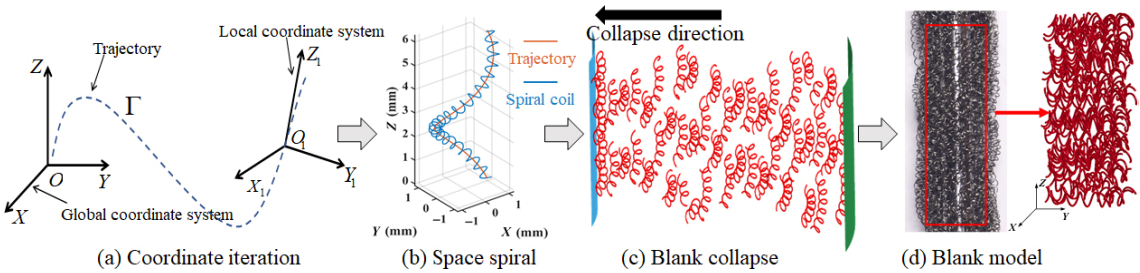

Fig. 3 CAT process route.

Table 1 Preparation parameters of FMP-MR.

Type	Wire diameter (mm)	Spiral diameter (mm)	Spiral pitch (mm)	Winding angle (°)	Number of winding layer	Number of windings per layer	Finished inner/outer diameter (mm)
Hollow ring	0.2	1.5	1.5	40	22	2	12/20
Solid cylinder	0.2	1.5	1.5	45	20	2	12/7

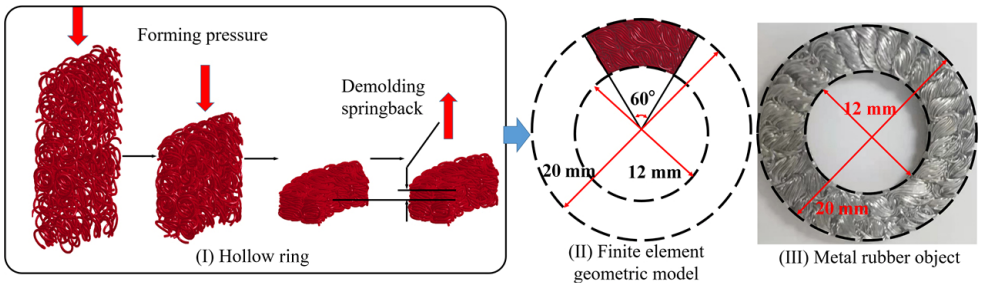

(a) Hollow ring forming process based on virtual manufacturing technology

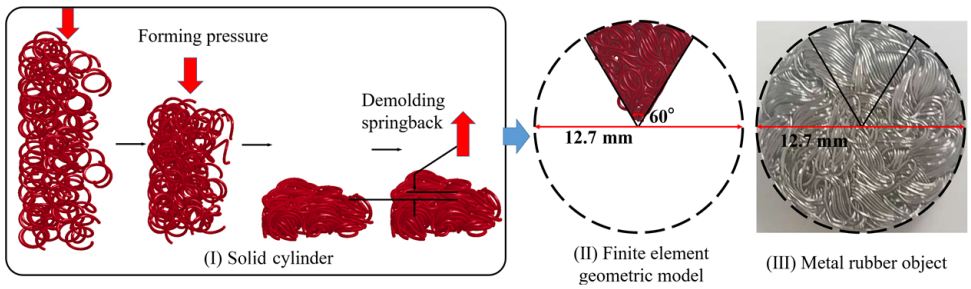

(b) Solid cylinder forming process based on virtual manufacturing technology

Fig. 4 Comparison of FMP-MR virtual stamping and actual test pieces.

indicated in Fig. 4, the FMP-MR finite element model was highly consistent with the actual FMP-MR specimen in both macroscopic morphology and meso-turn interlaced distributions. This confirmed the validity of the model established in this study.

Although the FMP-MR finite element model based on computer-aided preparation technology could reflect the real wire turn structure and texture distribution of materials, it would be difficult to discuss the quantitative relationships between the wire turn interaction of the spatial micropore structure and contact dry friction behavior. Therefore, through the construction of the finite element model, the spatial geometric coordinates of the FMP-MR internal wire turns are provided in the following.

2.2 Research on FMP-MR elastic force based on spatially randomly distributed microelements

The coordinate data of the FMP-MR finite element model of the previous section were extracted and discretized, and the spring microelements were constructed as randomly distributed in space. The random distribution of the microelements at any angle in space was used to randomly distribute the inner turns of the FMP-MR. The interpenetrating structure was effectively characterized and the random interpenetrating structure of the internal turns in FMP-MR was obtained by the random distribution of the microelements at an angle φ in space. Based on the spring theory, advanced material mechanics, and the Castigliano theory [28, 29], the stiffness of the microelement spring under only axial/radial load was obtained. A specific theoretical derivation can be found in Ref. [30].

$$\begin{cases} K_1 = \dfrac{F}{\Delta Z} = \dfrac{Ed^4}{4D\left[4D^2\cos\alpha\left(1+r\right)+\tan\alpha\sin\alpha\left(4D^2+d^2\right)\right]} \\ K_2 = \dfrac{F_r}{\Delta R} = \dfrac{2Ed^4\cos\alpha}{4D^3[(1+r)\sin^2\alpha+\cos^2\alpha+\pi^2\tan^2\alpha]+Dd^2\cos^2\alpha} \end{cases} \tag{1}$$

where D is the diameter of spiral coil, K_1 represents the stiffness of the axial microelement spring, K_2 is the stiffness of the meridional microelement spring, F denotes the axial load, F_r is the radial load, ΔZ refers to the axial deformation, ΔR is the radial deformation, d is the diameter of the metal wire material, E denotes the elastic modulus of the material, r is the Poisson's ratio, and α refers to the spiral angle of the microelement spring.

Based on the random distribution of spiral microelements at any angle, the internal force of the material was not only subjected to axial or radial loads but also closely related to the spatial distribution angle φ of spring microelements. Therefore, the spring microelement stiffness model with an arbitrary spatial angle distribution under the action of forming an external force was obtained by introducing the spatial distribution angle parameters of the microelement spring into the model as an important variable. In addition, the spatial distribution angle parameters $k(\varphi)$ were verified by Ma et al. [31] and our group's published literature [30].

$$k(\varphi)=\frac{F}{\Delta n}=\frac{2Ed^4\cos\alpha}{8D\sin^2\varphi(\omega_1(\alpha))+D\cos^2\varphi(\omega_2(\alpha))} \tag{2}$$

where $\Delta n=\Delta Z\sin\varphi+\Delta R\cos\varphi$, and $\omega_1=4D^2(1+r)\cos\alpha+\tan\alpha\sin\alpha(4D^2+d^2)$ and

$$\omega_2=\frac{4D^2+4D^2r\sin^2\alpha+d\cos^2\alpha+4\pi^2D^2\tan^2\alpha}{\cos\alpha}$$

represent the self-deformation parameters of the microelement spring unit under load.

The total stiffness per unit area of each layer $K(\varepsilon)$ can be obtained by assuming the existence of $L(\varepsilon)$ microelement springs on the unit area perpendicular to the forming direction and $m(\varepsilon)$ layer springs per unit length.

$$K(\varepsilon)=\sum_{i=1}^{L(\varepsilon)}k(\varphi,\alpha) \tag{3}$$

where the variables φ and α represent the spatial and temporal distribution characteristics of the spring microelements, respectively.

The total equivalent elastic stiffness of FMP-MR K_m^E can be calculated by placing the microelement springs between the layers.

$$K_m^E=\frac{\prod_{i=1}^{m(\varepsilon)}K_{iL}(\varepsilon)}{\sum_{i=1}^{m(\varepsilon)}\prod_{j=1,j\neq i}^{m(\varepsilon)}K_{iL}(\varepsilon)}=\left(\sum_{i=1}^{L(\varepsilon)}K(\varphi,\alpha)\right)/m(\varepsilon) \tag{4}$$

By assuming the number of the microelement springs per unit volume through Eq. (4), Eqs. (5)–(6) can be obtained.

$$L(\varepsilon)=\left(\frac{4\bar{\rho}_m(\varepsilon)}{\pi^2Dd^2}\right)^{\frac{2}{3}} \tag{5}$$

$$\frac{L(\varepsilon)}{m(\varepsilon)}=\left(\frac{4\bar{\rho}_m(\varepsilon)}{\pi^2Dd^2}\right)^{\frac{1}{3}} \tag{6}$$

where $\bar{\rho}_m$ is the relative density of FMP-MR, $\bar{\rho}_m(\varepsilon)=\frac{\rho_m(\varepsilon)}{\rho}$; ρ_m represents the density of the FMP-MR material and ρ refers to the linear density of silk.

By introducing the shape factor $C=L/A$, where L represents the height of the FMP-MR and A is the cross-sectional area of the FMP-MR perpendicular to the forming direction, the combination of the above formulas yields the mapping relationship between the FMP-MR total elastic force K_m and strain of under the load in the forming direction.

$$K_m(\varepsilon)=\frac{L}{A}\left(\frac{4\bar{\rho}_m(\varepsilon)}{\pi^2Dd^2}\right)^{-\frac{1}{3}}\sum_{i=1}^{L(\varepsilon)}K(\varphi,\alpha) \tag{7}$$

2.3 Numerical reconstruction of FMP-MR dynamic contact dry friction of complex structure based on cell group model

The cell group model is a dynamic system used to perform the quasi-linear reconstruction of highly nonlinear discrete structures based on the differential remodeling theory using dynamic discretization of the spatial model [32]. The improvement in discrete microelement accuracy could significantly increase the search efficiency of the model contact behavior and comprehensively restore the real space dynamic contact state of wire turns in FMP-MR. Therefore, the cell group model can be effectively used to accurately determine the spatial behavior of complex configurations.

Figure 5 displays the establishment of the cell series group numerical model based on the FMP-MR space wire turn structure (see the finite element model in Section 2.1) through virtual reconstruction of the linear micro-segment. The main cell and experimental cell vectors can be defined under different conditions by considering the different and parallel planes of the cell groups between different spiral volumes. The main cell vector can be defined as the cell vector actively participating in the contact boundary search, whereas the experimental cell vector can be viewed as the cell vector passively participating in the contact boundary search.

2.3.1 *Different faces of cell group (including intersections)*

The principal cell vector $\vec{DV}_i(x,y,z)$ can be expressed based on Eq. (8).

$$\vec{DV}_i(x,y,z) = \mathrm{Sub}_{i+1}(x_b,y_b,z_b) - \mathrm{Sub}_i(x_a,y_a,z_a) \quad (8)$$

where $\mathrm{Sub}_{i+1}(x_b,y_b,z_b)$ is the spatial coordinate of the tail end of the main cell, and $\mathrm{Sub}_i(x_a,y_a,z_a)$ refers to the spatial coordinates of the head end of the main cell.

In addition, the test cell vector ($\vec{DV}_i'(x,y,z)$) is given by Eq. (9).

$$\vec{DV}_i'(x,y,z) = O_{b_{i+1}}(x_d,y_d,z_d) - O_{b_i}(x_c,y_c,z_c) \quad (9)$$

where $O_{b_{i+1}}(x_d,y_d,z_d)$ denotes the spatial coordinate of the tail end of the test cell, and $O_{b_i}(x_c,y_c,z_c)$ is the spatial coordinate of the head end of the test cell.

The common perpendicular vector of the principal and test cell vectors ($\vec{VV}_i(x,y,z)$) can be obtained based on Eq. (10).

$$\vec{VV}_i(x,y,z) = \vec{DV}_i(x,y,z) \times \vec{DV}_i'(x,y,z) \quad (10)$$

Any vector can be defined following Eq. (11).

$$\vec{ArV}_i(x,y,z) = O_{b_i}(x_c,y_c,z_c) - \mathrm{Sub}_i(x_a,y_a,z_a) \quad (11)$$

The vector projection on the common vertical line was performed based on the space vector projection method to yield the minimum distance between cell groups.

$$\mathrm{Distance} = \frac{\left|\vec{VV}_i \cdot \vec{ArV}_i\right|}{\vec{VV}_i} \quad (12)$$

2.3.2 *Parallel cell groups (including coincidence)*

In this case, the formula in Eq. (13) can be obtained.

$$\vec{DV}_i(x,y,z) = R \cdot \vec{DV}_i'(x,y,z) \quad (13)$$

where R is a real number.

$$\vec{ArV}_i(x,y,z) = R \cdot O_{b_i}(x_c,y_c,z_c) - \mathrm{Sub}_i(x_a,y_a,z_a) \quad (14)$$

$$\mathrm{Distance} = \frac{\left|\vec{ArV}_i(x,y,z) \cdot \vec{DV}_i(x,y,z)\right|}{\left|\vec{DV}_i(x,y,z)\right|} \quad (15)$$

Based on the determined minimum distance of the cell group, the contact space of the cell group model can be accurately located and searched. By assuming the spatial contact point between the main and experimental cells as $M(x_m,y_m,z_m)$ and $N(x_n,y_n,z_n)$, respectively, Eqs. (16) and (17) can be obtained as

$$M(x_m,y_m,z_m) - \mathrm{Sub}_i(x_a,y_a,z_a) = t_1 \cdot \vec{DV}_i(x,y,z) \quad (16)$$

$$M(x_m,y_m,z_m) = t_1 \cdot \vec{DV}_i(x,y,z) + \mathrm{Sub}_i(x_a,y_a,z_a) \quad (17)$$

Similarly, Eq. (18) can be formulated as

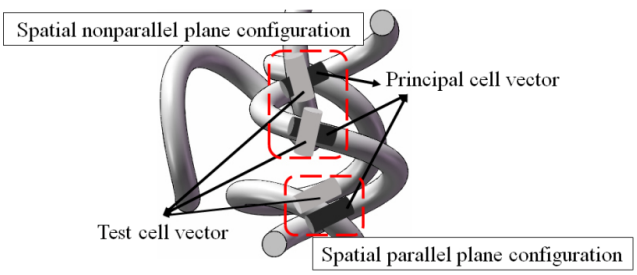

Fig. 5 Schematic diagram of FMP-MR cell group model.

$$N(x_n, y_n, z_n) = t_2 \cdot \vec{DV_i}'(x,y,z) + O_{b_i}(x_c, y_c, z_c) \quad (18)$$

where t_1 and t_2 are proportional coefficients.

According to the common vertical line theorem, the vector $\vec{MN}(x,y,z)$ should be perpendicular to both the main and test cells. Therefore, Eqs. (19) and (20) can be obtained based on the point product characteristics of the space vector.

$$\vec{DV_i}(x,y,z) \cdot \vec{MN}(x,y,z) = 0 \quad (19)$$

$$\vec{DV_i}'(x,y,z) \cdot \vec{MN}(x,y,z) = 0 \quad (20)$$

These equations can be further simplified by Eqs. (21)–(25).

$$F_1 = (x_b - x_a)^2 + (y_b - y_a)^2 + (z_b - z_a)^2 \quad (21)$$

$$F_1' = (x_d - x_c)^2 + (y_d - y_c)^2 + (z_d - z_c)^2 \quad (22)$$

$$F_2 = (x_b - x_a)(x_d - x_c) + (y_b - y_a)(y_d - y_c) + (z_b - z_a)(z_d - z_c) \quad (23)$$

$$F_3 = (x_b - x_a)(x_c - x_a) + (y_b - y_a)(y_c - y_a) + (z_b - z_a)(z_c - z_a) \quad (24)$$

$$F_3' = (x_d - x_c)(x_c - x_a) + (y_a - y_c)(y_c - y_a) + (z_d - z_c)(z_c - z_a) \quad (25)$$

Simultaneous upper type would lead to Eq. (26).

$$t_1 = \frac{F_3 \cdot F_1' - F_3' \cdot F_2}{F_1 \cdot F_1' - F_2^2}, \quad t_2 = \frac{F_3' \cdot F_1 - F_2 \cdot F_3}{F_2^2 - F_1 \cdot F_1'} \quad (26)$$

To date, the cell group contact search has been completed based on $M(x_m, y_m, z_m)$ and $N(x_n, y_n, z_n)$,

where

$$x_m = \frac{(x_b - x_a) \cdot (F_3 \cdot F_1' - F_3' \cdot F_2)}{F_1 \cdot F_1' - F_2^2} + x_a$$

$$y_m = \frac{(y_b - y_a) \cdot (F_3 \cdot F_1' - F_3' F_2)}{F_1 \cdot F_1' - F_2^2} + y_a$$

$$z_m = \frac{(z_b - z_a) \cdot (F_3 \cdot F_1' - F_3' \cdot F_2)}{F_1 \cdot F_1' - F_2^2} + z_a$$

$$x_n = \frac{(x_d - x_c) \cdot (F_3' \cdot F_1 - F_3 \cdot F_2)}{F_2^2 - F_1 \cdot F_1'} + x_c$$

$$y_n = \frac{(y_d - y_c)(F_3' \cdot F_1 - F_3 \cdot F_2)}{F_2^2 - F_1 \cdot F_1'} + y_c$$

$$z_n = \frac{(z_d - z_c)(F_3' \cdot F - F_3 \cdot F_2)}{F_2^2 - F_1 \cdot F'} + z_c$$

The accurate positioning of the contact area of the cell group model in space could then be completed by establishing the above model. However, because the contact dry friction of the wire turns in FMP-MR was considered as a sequential dynamic process, the time dimension parameter (Distance$_t$) was introduced into the spatial dimension of the contact area to complete the contact slip determination under dynamic timing (Eq. (27)).

$$\begin{cases} \text{Distance}_t > 0.2 \Rightarrow \text{non-contacted} \\ \text{Distance}_t \leqslant 0.2 \Rightarrow \begin{cases} \text{Distance}_{t+1} > 0.2 \Rightarrow \text{spatial detachment} \\ \text{Distance}_{t+1} \leqslant 0.2 \Rightarrow \begin{cases} M_{t+1}(x_m, y_m', z_n') - M_t(x_m, y_m, z_n) \\ \quad = N_{t+1}(x_n', y_n', z_n') - N_t(x_n, y_n, z_n) \\ \quad \Rightarrow \text{viscous extrusion} \\ M_{t+1}(x_m', y_m', z_m') - M_t(x_m, y_m, z_m) \\ \quad \neq N_{t+1}(x_n', y_n', z_n') - N_t(x_n, y_n, z_n) \\ \quad \Rightarrow \text{sliding friction} \end{cases} \end{cases} \end{cases} \quad (27)$$

In Eq. (27), the spatial separation and stick extrusion of the contact area in the dual dimensions of time and space, in addition to the separation of spatial physical contact or sliding distance in the direction of the friction load between cell groups, generated less energy under the excitation of an external load coupled with a small contribution of such characteristic contact to the FMP-MR damping energy dissipation behavior. Such contact could be defined as an invalid contact (Fig. 6(a)). The physical characteristic area of the spatial contact slip was maintained between cell groups under the time series. This part of the contact can be considered as the fundamental factor causing friction energy consumption (Fig. 6(b)), which contributes significantly to the damping energy dissipation capacity of the entire material. After obtaining effective contact between the turns in the above material, the influencing

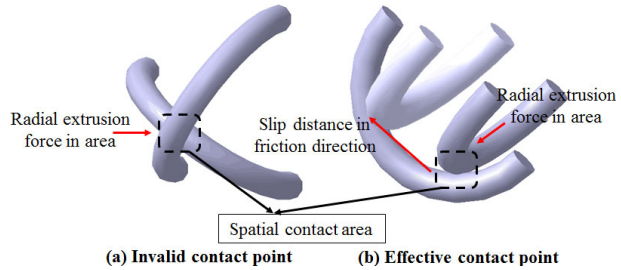

Fig. 6 Schematic diagram of contact points.

parameters under the damping energy dissipation mechanism were further refined.

In practice, large numbers of spatial contact points would exist between the inner turns of the FMP-MR. The micro contact areas of the turns generated from the internal physical boundary constraints of the material can be divided into two categories: 1) ineffective contact points that cannot be relatively slipped (Fig. 6(a)) and 2) effective contact points that can be relatively slipped and dry frictional (Fig. 6(b)). By combining Eq. (27) and capturing the dynamic behavior of the spatial microstructure of the cell group in time series, the dynamic evolution of the internal spatial physical contact distribution and effective contact distribution in the FMP-MR time domain can be deeply explored. An interesting quasi-Gaussian distribution contact behavior was discovered in this work, and an effective stick slip coefficient was proposed to further describe the meso-contact distribution characteristics based on Eq. (28).

$$\eta = N_e / N_T \tag{28}$$

where η is the effective stick slip coefficient; N_e is the number of effective contact points; N_T is the number of spatial contact points.

η can be used to describe the proportion of the effective contact points of the random contact points in the FMP-MR space, which has a decisive role in the energy consumption characteristics of FMP-MR. The changes in the contact point distribution with time series of hollow ring and solid cylinder FMP-MR under quasi-static loading and unloading load in the forming direction are displayed in Figs. 7 and 8. Here, the labeled Figs. 7(b)–7(e) represent the spatial distribution diagrams of the effective and invalid contact points, and Fig. 7(e) illustrates the time-series changing curves of the contact point distribution behavior and effective stick slip coefficient. As indicated in Figs. 7(a) and 8(a), a certain number of spatial contact points existed between the turns of the FMP-MR before loading (t = 0 s). However, the relative dry frictional slip motion between the turns did not occur because no load was applied at this time, and the number of effective contact points was set to zero. Thus, all invalid contact points are visible in Figs. 7(b) and 8(b). Under the continuous action of external load in the forming direction, the number of both spatial and effective contact points increased significantly owing to the continuous shrinkage of the pores in FMP-MR and gradual reduction of "free" motion space between wire turns. Conversely, the number of invalid contact points first increased and then decreased. Moreover, the number only changed minimally during the loading process (Figs. 7(b)–7(e) and 8(b)–8(e)), causing the finite contact point to

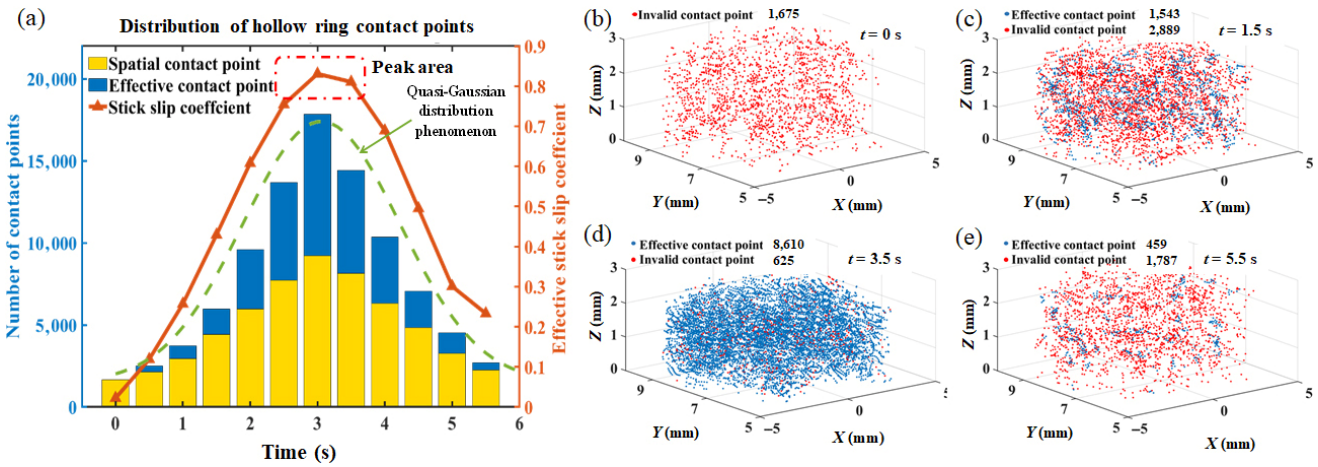

Fig. 7 Variation of contact point distribution of hollow ring FMP-MR as a function of time series. (a) Distribution of contact points; (b)–(e) Number distribution of effective contact points and invalid contact points.

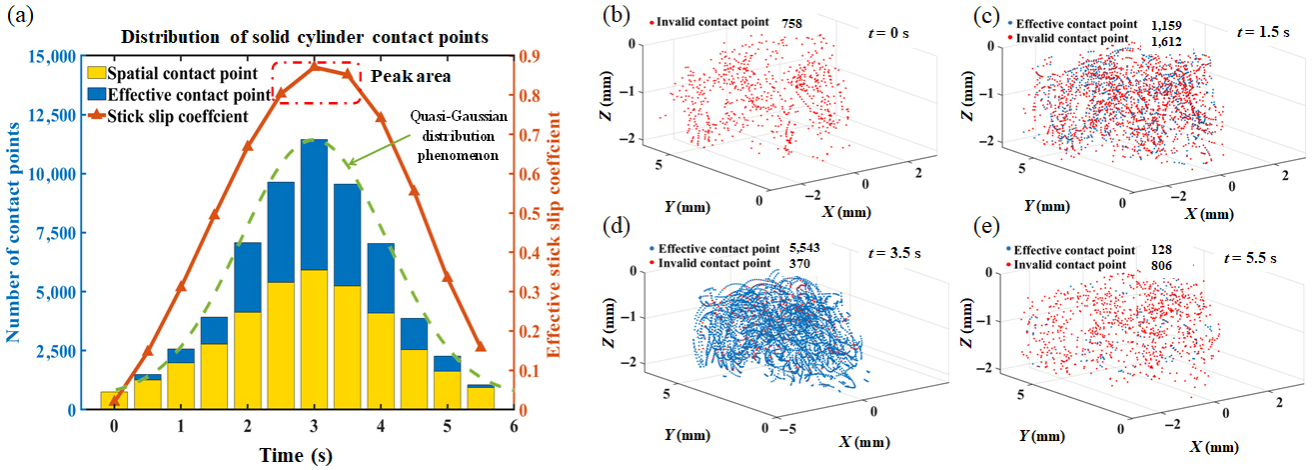

Fig. 8 Variation of FMP-MR contact point distribution of solid cylinder as a function of time series. (a) Distribution of contact points; (b)–(e) Number distribution of effective contact points and invalid contact points.

gradually approach the number of spatial contact points under the load action. After reaching the load limit (t = 3 s), the effective contact points reached a peak with the number equal to that of the spatial contact points.

The effective stick slip coefficient curve (indicated by the red dotted line in Figs. 7(a) and 8(a)) demonstrated a gradual increase from zero to the load limit moment during load application, achieving a peak area. During the unloading process, the FMP-MR gradually lost the load constraint in the forming direction. Moreover, the inner turns rebounded gradually, whereas different degrees of dry friction slip of the turns occurred. However, the "free" movement space of the turns increased with the gradual recovery of the internal pores in the material, and the numbers of spatial contact points and effective contact points indicated different reduction trends. Simultaneously, the quasi-Gaussian distribution phenomenon of FMP-MR turn contact behavior (Figs. 7(a) and 8(a)) under sequential loading exhibited a peak distribution in the load limit stage area. The mathematical expectation and variance of its distribution function were different from those of the traditional Gaussian distribution. The contact point distribution behavior of FMP-MR presented clear asymmetric characteristics owing to the influence of numerous factors including the FMP-MR material preparation process and internal topology.

The distribution number of effective contact points inside the FMP-MR and changing trend of the effective stick slip coefficient revealed that the number of effective contact points inside the material gradually approached the total number of spatial contact points under load. In addition, the effective stick slip coefficient gradually approached one. Under the action of the micro contact dry friction of the wire turns, the small effective contact areas produced large amounts of slip energy dissipation. The latter can be considered an important factor in the damping hysteresis energy consumption characteristics of the material. Therefore, the spatial dry friction slip vector positioning the effective contact point in the contact area was completed by determining the contact slip vector equation (Eq. (27)). Moreover, the contact friction between the cell group and microelement was obtained by calculating the normal contact force of the main cell. These steps were used to analyze the dry friction energy between the material cell groups.

The space displacement vector of the effective contact ($\overline{s_i}$) can be expressed using Eq. (29).

$$\begin{aligned}\overline{s_i} = &\left(M_{t+1}\left(x'_m, y'_m, z'_m\right) - M_t\left(x_m, y_m, z_m\right)\right) \\ &-\left(N_{t+1}\left(x'_n, y'_n, z'_n\right) - N_t\left(x_n, y_n, z_n\right)\right)\end{aligned} \tag{29}$$

The normal displacement vector of the principal cell on a common vertical line (Δh_i) is given by Eq. (30).

$$\Delta h_i = \frac{\left|\left(M_{t+1}\left(x'_m, y'_m, z'_m\right) - M_t\left(x_m, y_m, z_m\right)\right)\cdot\left(M_{t+1}\left(x'_m, y'_m, z'_m\right) - N_{t+1}\left(x'_n, y'_n, z'_n\right)\right)\right|}{\left|M_{t+1}\left(x'_m, y'_m, z'_m\right) - N_{t+1}\left(x'_n, y'_n, z'_n\right)\right|} \tag{30}$$

The normal force of the principal cell (F_{N_i}) can be summarized using Eq. (31).

$$F_{N_i} = k_{2i}(\varphi) \cdot \Delta h_i \tag{31}$$

When the FMP-MR is subjected to an external load, the internal turns undergo spatial displacement and deformation. With the continuous reduction of the internal pores of the FMP-MR, contact friction occurs gradually between the turns. When the friction force reaches the maximum static friction force, relative motion occurs between the relatively static turns, and the static friction force is converted into a sliding friction force. Even a small relative movement induces energy dissipation because of the partial slip at the contact boundary, especially in such a point contact. However, as a model, one can neglect this part and consider only the case of gross slip. Moreover, the dynamic friction caused by the surface roughness of the turns was small. Therefore, in this study, the sliding friction considers only the dynamic sliding friction coefficient and normal load. The principal cell contact friction ($F_{f_i}(x,y,z)$) can be expressed using Eq. (32).

$$F_{f_i}(x,y,z) = \mu F_{N_i} \tag{32}$$

where μ is the sliding friction coefficient, which is defined as 0.32 in this study.

The energy accumulation of the wire turn microelement (ΔE) can be calculated using Eq. (33).

$$\Delta E = \sum_{i=1}^{L(\varepsilon)\cdot m(\varepsilon)} \left(F_{f_i} \cdot \overline{s}_i \right) \tag{33}$$

The squeezing and slippage between the microelements of the internal turns in FMP-MR produced a local spatial displacement vector ablation in the topological structure of its numerous turns. Hence, the spatial dry frictional displacement generated by the large number of effective contact points between the FMP-MR turns was gradually filled and accommodated by the pores in the micropore physical structure. This led to mutual cancellation, whereas energy loss remained a cumulative process. Therefore, the changes in the FMP-MR load in the hysteresis curve under the overall deformation of the load depended not only on the linear summation process of dry friction but also on the effective contact point of the material turns and dry friction slip. Based on the statistics for the dry friction slip distance in Eq. (29), the contact friction displacement between wire turns in the material presented a gap estimated to be 5–6 times the forced FMP-MR vibration displacement owing to the displacement ablation phenomenon in the local space. Therefore, the concept of equivalent frictional damping force was defined, and the energy loss mechanism of the internal structure in the fretting slip state was characterized by the overall material vibration.

The equivalent friction damping force (F_E) can be expressed by Eq. (34).

$$F_E = \frac{\Delta E}{\Delta S} \tag{34}$$

where ΔS is the displacement microelement under the total FMP-MR load.

The overall elastic restoring force ($F_{ES}(\varepsilon)$) may be calculated by Eq. (35).

$$F_{ES}(\varepsilon) = k_{mn}(\varepsilon) \cdot \varepsilon / A \tag{35}$$

Thus, the energy dissipation hysteresis model can be obtained through the study of the FMP-MR multiscale dry friction damping energy dissipation mechanism,

$$\begin{cases} F_1 = F_{ES}(\varepsilon) + F_E(\varepsilon) \\ F_2 = F_{ES}(\varepsilon) - F_E(\varepsilon) \end{cases} \tag{36}$$

where F_1 is the force of the loading curve and F_2 is the force of the unloading curve.

3 Study of FMP-MR spatial distribution energy consumption

The time-serie evolution behaviors of fretting friction displacement, tangential friction, and dry friction energy consumption at the effective contact point of FMP-MR are discussed in detail in the above sections. However, the distribution of the dry friction energy generated by FMP-MR in space as a multipoint randomly distributed material with a spatial microporous structure is critical to the overall energy dissipation characteristics of the material. Therefore,

the hollow and solid cylinders obtained from the above computer-aided preparation were subjected to the finite element analysis. In addition, the FMP-MR dry friction mechanism based on the internal wire turn energy dissipation in a multidimensional spatial distribution was investigated by subjecting the model to a dynamic numerical reconstruction based on a cell group. Because FMP-MR dissipates the maximum energy value under the ultimate load, the spatial distribution of the energy consumption of the material was discussed in subsequent research and analysis using FMP-MR at the initial stage of load (0.2 mm in the forming direction) under the maximum displacement load (0.6 mm in forming direction).

From this study, the dry friction energy clouds of the hollow ring and solid cylinder FMP-MRs in spatial contact under load and the equivalent force clouds in CAT are displayed in Figs. 9 and 10. In the initial load action stage, numerous internal pores with large spaces in the FMP-MR can be observed. The majority of the load actions realized the overall deformation through pore filling, and the number of effective contact points between the material turns was small. These features resulted in a small number of energy-dissipating areas. Under continuous application of the load, the free space available for the movement of the wire turns inside the FMP-MR was drastically reduced, resulting in numerous contact friction phenomena. This significantly enhanced the amount of frictional energy generated inside the material, as indicated in Table 2.

The distributions of the contact friction energy loss for different values in FMP-MR are illustrated in Figs. 9 and 10. The spatial position of the energy generation was mainly concentrated near the contact points between wire turns in the FMP-MR, where the distribution was highly consistent with the spatial distribution of the FMP-MR contact points [30].

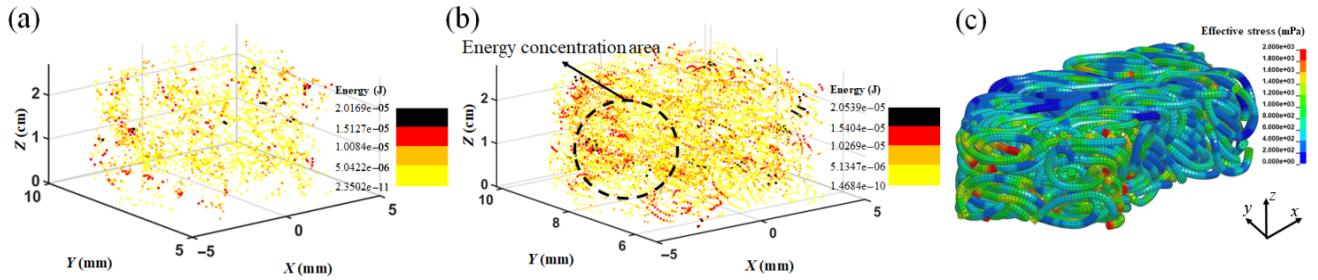

Fig. 9 Four-dimensional (4D) diagram of dry friction energy dissipation and finite element stress analysis diagram (1/6 hollow ring). (a) Initial load stage, (b) ultimate load stage, and (c) cloud chart of equivalent stress distribution (ultimate load stage).

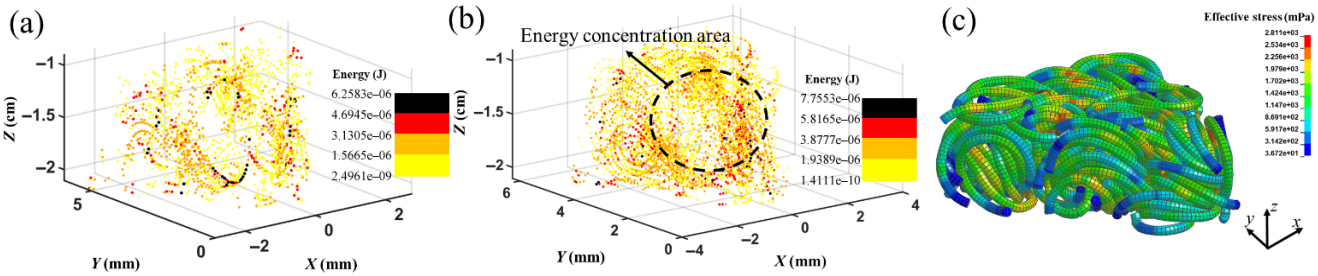

Fig. 10 4D diagram of dry friction energy dissipation and finite element stress analysis diagram (1/6 solid cylinder). (a) Initial load stage, (b) ultimate load stage, and (c) cloud chart of equivalent stress distribution (ultimate load stage).

Table 2 Statistical diagram of the number of effective contact points.

Loading stage	Number of effective contact points		
	Hollow ring (single wire turn)	Hollow ring (integral)	Solid cylinder (integral)
Initial	77	2,453	1,585
Ultimate	225	8,610	5,543

In addition, the cumulative effect of the energy consumption of tens of thousands of effective contact points collectively resulted in the excellent dry friction damping characteristics of the metal–rubber material, despite the low energy dissipation at a single effective contact point (10^{-6} to 10^{-5}). In Figs. 9(c) and 10(c), the red area in the FMP-MR stress cloud represents the stress concentration area between the turns of the wire. A closer energy cloud diagram to the black or red area led to a greater energy generation position, consistent with the FMP-MR inter-turn stress concentration area. The reason for this was related to the friction coefficient and the increase in sliding friction between the wire turns with normal contact load, resulting in greater energy loss. Moreover, the greater normal contact load and tangential friction force led to enhanced contact stress between turns, which is conducive to the occurrence of the stress concentration phenomenon. The regional distribution diagram of the single-turn energy extracted from a hollow ring is displayed in Fig. 11.

As indicated in Fig. 11(a), the pore filling between the wire turns in the material during the initial loading stage is the primary action. In addition, fewer wire turn spiral coils demonstrated the contact dry friction behavior, resulting in less energy generation area around them. Moreover, the FMP-MR continuous compression deformation under load led to the gradual disappearance of the micropore structure between the internal wire turns. Hence, the dry friction sliding contact between the wire turns accounted for the main proportion, resulting in a significant increase in the amount of friction energy consumption. In particular, the energy was generated in the contact slip surface area of the wire turns owing to a certain degree of contact dry friction slip between the wire turns and adjacent wire turns under the action of an external load (Fig. 11). This resulted in material surfaces with varying degrees of energy dissipation dominated by thermal energy loss.

To further refine the FMP-MR energy dissipation mechanism, the dry friction displacement and energy generated by a hollow ring FMP-MR in 3D space were projected onto the *XOY* plane and *X*-axis. As indicated in Fig. 12, the overall displacement distribution is relatively uniform. The fewer inter-turn constraints in the material boundary area maintained a step phenomenon of contact friction in the wire turn boundary area [27]. The disordered multipoint random contact characteristics of the wire turn space in the overall FMP-MR structure resulted in static friction reaching a certain saturation value under the action of an external force. In addition, micro slip occurred as this turned to slide friction with the corresponding energy distribution tending to be consistent (Figs. 12(b) and 12(d)). In particular, the value of the inter-turn energy dissipation on the premise of a constant material contact friction coefficient and a constant normal contact size was directly proportional to the contact slip distance of the material. Therefore, the spatial dry friction slips of the contact points on each wire turn in FMP-MR effectively reflected the energy consumption to a certain extent.

The projection of the spatial displacement of single-turn dry friction and its actual dissipated energy in the XOY plane and *X*-axis are indicated in Fig. 13. As the inter-turn interaction constraints reduced (Figs. 13(a) and 13(c)), the dry friction displacement of the wire turns in the boundary region appeared in the form of a local step. The 2D and one-dimensional (1D) distribution diagrams of the energy generated by single-turn dry friction are displayed in Figs. 13(b) and 13(d), respectively. These changes were consistent with the trend of spatial displacement. The energy

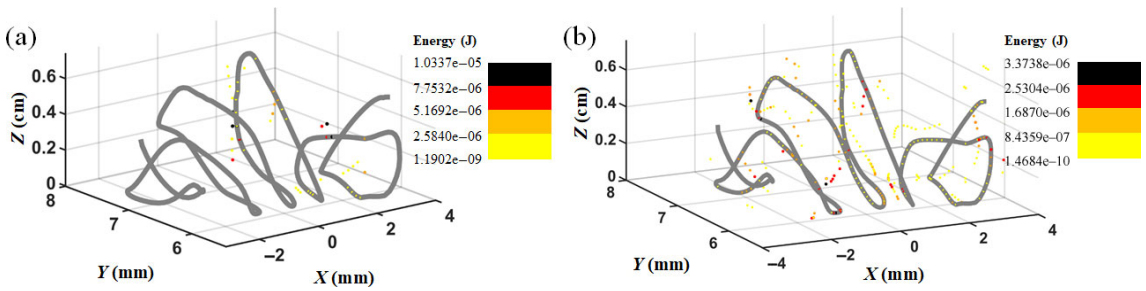

Fig. 11 4D diagram of single turn dry friction energy dissipation. (a) Initial load stage and (b) ultimate load stage.

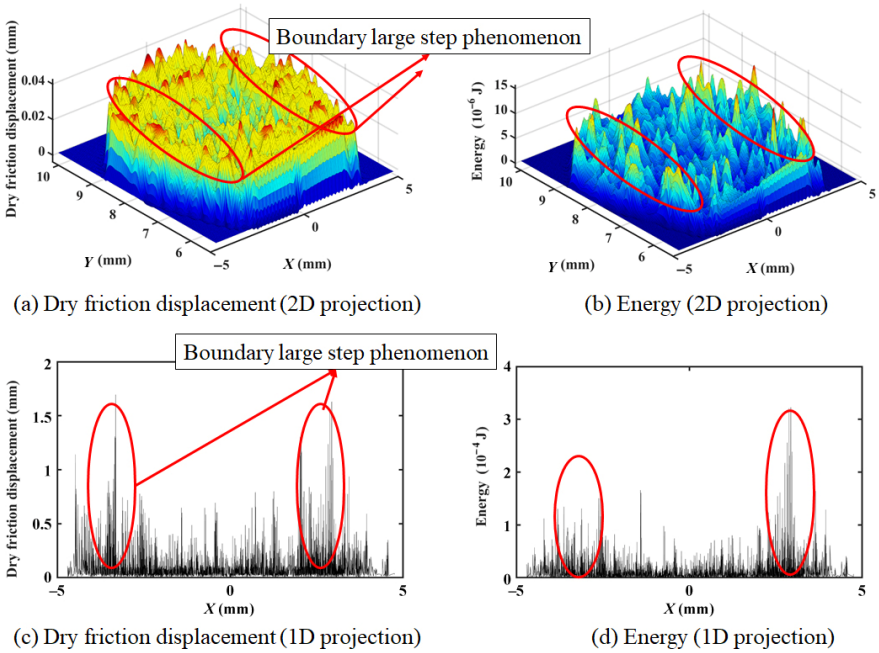

(a) Dry friction displacement (2D projection) (b) Energy (2D projection)

(c) Dry friction displacement (1D projection) (d) Energy (1D projection)

Fig. 12 2D and 1D projection of displacement vectors and energy distributions of annular FMP-MR dry friction.

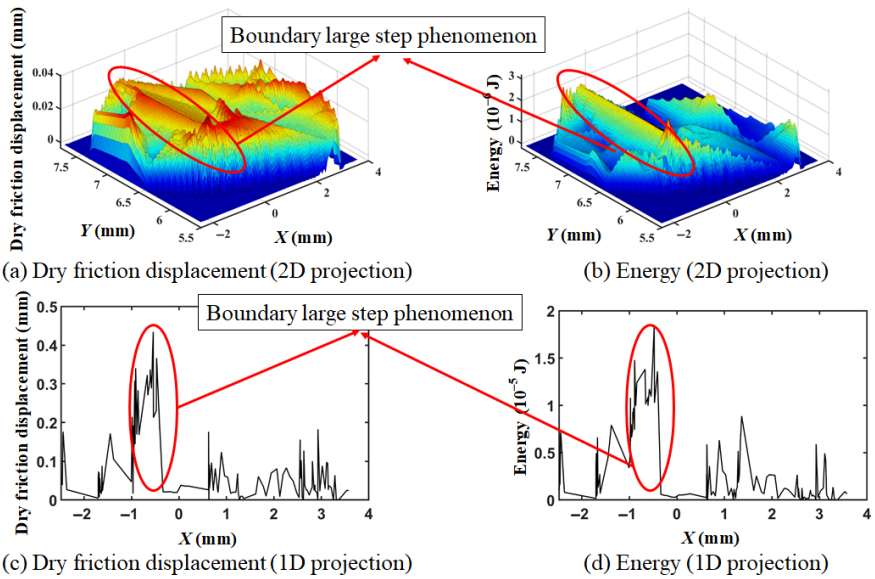

(a) Dry friction displacement (2D projection) (b) Energy (2D projection)

(c) Dry friction displacement (1D projection) (d) Energy (1D projection)

Fig. 13 2D and 1D projection of spatial displacement vectors and energy distributions of single-turn dry friction.

achieved its greatest value during the occurrence of slip. Simultaneously, the friction displacement of a single wire turned in space, and the energy value generated by it, both demonstrated heave rolling in the plane projection. This can be attributed to the complex and irregular spatial geometric topology of FMP-MR, in addition to the disordered distribution of the contact position and contact friction state between the wire turns in space. Therefore, the energy distribution in the plane was not uniform and orderly.

In summary, subjecting the spatial microporous material with a wire turn disordered grid interpenetrating structure to external load largely depended on the load energy internal friction in the form of dry friction at the effective contact point between the internal wire turn spiral coils in fretting friction displacement. To further verify the accuracy of the model developed in this study, subsequent experiments

were performed to determine the macroscopic properties of the material.

4 Experimental verification and results and discussion

4.1 Experimental process

Hollow rings and solid cylinders were used to study the physical preparation of FMP-MR based on the preparation process parameters listed in Table 1. The raw material was 304 (06Cr19Ni10) austenitic stainless steel wire based on the cold drawing process. After completion of the blank preparation by numerical control (NC) blank winding, the blank was placed in the designed stamping die for limited tonnage stamping in a THD32-100 four-column hydraulic press to ensure the dimensional parameters of the prepared FMP-MR. As indicated in Fig. 4, the distribution of the wire turn structure was highly consistent with the computer-aided preparation model. To ensure the effectiveness of the experiment, several groups of hollow ring and solid cylinder FMP-MRs were prepared in this study, as indicated in Fig. 14(b).

The prepared FMP-MR was then placed in a WDW-T200 microcomputer-controlled electronic universal testing machine (made in Jinan Tianchen Testing Machine Manufacturing Co., LTD., China) for limited displacement loading and unloading. The maximum test force of the tester was set to 200 kN, the displacement of the beam was 0–600 mm, the movement speed was from 0.01 to approximately 500 mm/min, and the resolution of the deformation was 0.001 mm. In this work, the test load was performed by setting the FMP-MR molding upward to apply a displacement load of 0.6 mm and at a loading rate of 2 mm/min. The changes in the force and displacement of the sensor during loading and unloading were recorded in real time. Five groups of FMP-MR quasi-static compression test data with the same parameters were averaged to ensure the effectiveness and repeatability of further tests. The hysteresis curves derived from the test and dynamic simulations were then compared and analyzed. The quasi-static loading and unloading processes are displayed in Fig. 14(a).

4.2 Results and discussion

The FMP-MR dry friction damping hysteresis constitutive model based on the cell group energy dissipation mechanism was prepared through FMP-MR tests with different shapes. The data were then compared and analyzed in combination with the load–deformation curves of the quasi-static compression tests.

As indicated in Fig. 15, the configuration of the hollow ring induced FMP-MR with a hollow structure near the inner diameter, fewer physical constraints between the surrounding wire turns, and self-elastic behavior of the wire turn spiral coil, which were more prominent than those of the solid cylinder FMP-MR. Therefore, the dry friction ratio of the wire was relatively reduced, and the hysteresis curve of the FMP-MR with the hollow ring configuration indicated a slender shape. The solid cylinder FMP-MR illustrated a large amount of frictional energy dissipation mechanism owing to the significant dry friction phenomenon inside the material. This led to a larger hysteresis fallback in the unloading curve when

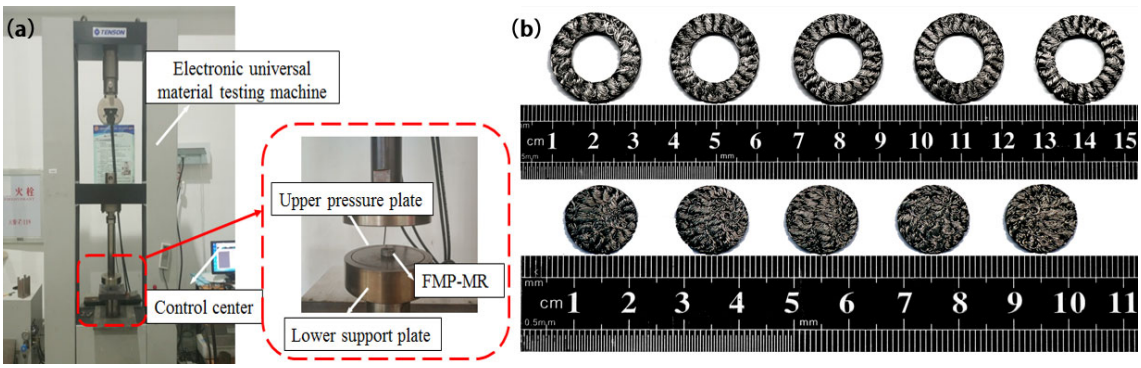

Fig. 14 FMP-MR quasi-static loading and unloading test.

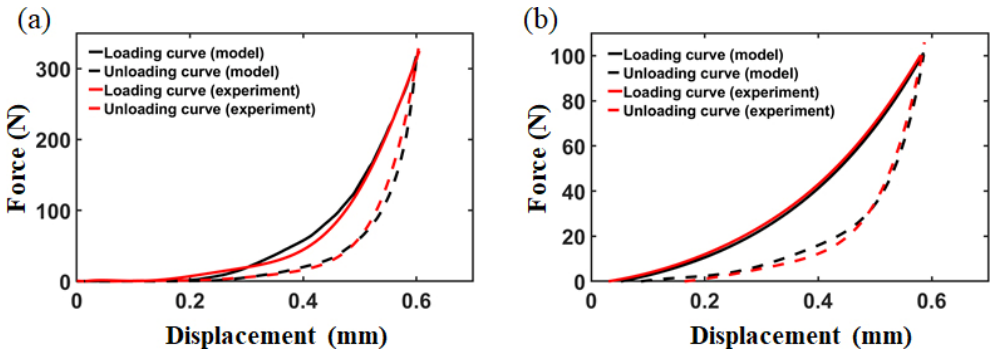

Fig. 15 Hysteresis loop verification. (a) Hollow ring and (b) solid cylinder.

compared to the loading curve, with a relatively "bloated" hysteresis curve shape (Fig. 15(b)). In summary, the different distribution laws of internal turns in FMP-MR under different configurations led to significantly different contact dry friction energy consumption behaviors between the structures on the meso-scale. Under the same input of external environmental energy, the damping characteristics of the solid cylinder FMP-MR were excellent.

The distribution of the FMP-MR energy dissipation in 2D and 3D space is important for studying the dry friction damping hysteresis characteristics of materials. Moreover, the cumulative law of the generation and dissipation of energy consumption is highly related to time. The phased energy dissipation and cumulative dissipation curves of the experimental tests and numerical modeling under a 0.6 mm alternating load are displayed in Figs. 16 and 17. Under a continuous applied load (Fig. 16), the effective contact points inside the material increased significantly, and the generated energy loss indicated an increasing trend. However, the FMP-MR phased energy dissipation peak was not in the limit load area, indicating a greater number of effective contact points with a certain hysteresis. The reason for this is related to the energy loss mechanism in the material, which was not limited to the number

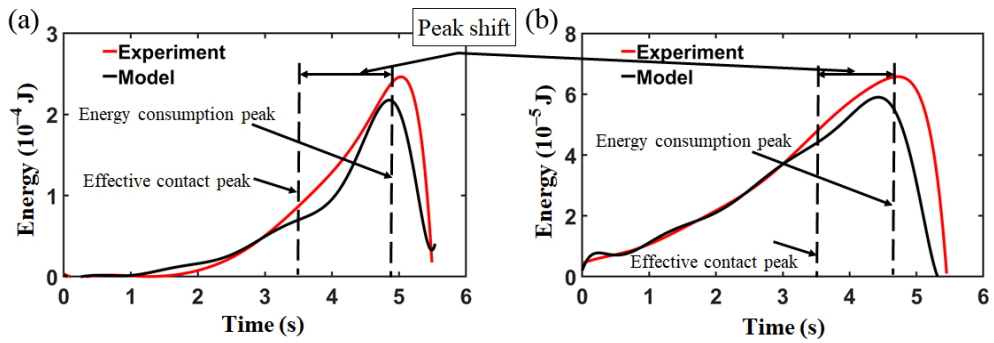

Fig. 16 Displacement stage performance consumption verification. (a) Hollow ring and (b) solid cylinder.

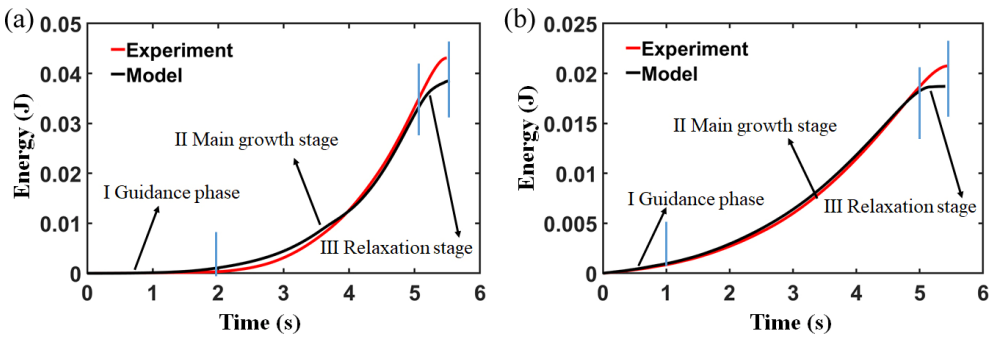

Fig. 17 Displacement energy consumption verification. (a) Hollow ring and (b) solid cylinder.

of effective contact points. The unloading process after the limit load to a certain extent, led to the rebounding of the wire turns in the FMP-MR. The released pores met the spatial motion region of the wire turns, and the dry friction slip between the wire turns increased significantly. Overall, the FMP-MR damping energy dissipation mechanism was closely related to the effective contact points inside the material in addition to its dry friction micro-displacement.

Tables 3 and 4 list the residual analysis and energy relative error analysis of the hysteresis curves, respectively. For the residual analysis, the effectiveness of the model was quantitatively measured by calculating the correlation index. A correlation index closer to one would lead to a greater prediction accuracy of the model equation and stronger linear correlation between the actual observation variables and prediction variables. The calculation formula for the residual analysis R^2 can be given by Eqs. (37)–(39).

$$RSS = \sum_{i=1}^{n} (y_i - \hat{y}_i)^2 \tag{37}$$

$$TSS = \sum_{i=1}^{n} (y_i - \overline{y})^2 \tag{38}$$

$$R^2 = 1 - \frac{RSS}{TSS} \tag{39}$$

where RSS is the sum of squares of the residuals; TSS refers to the sum of the total squares; n is the number of sample observations; y_i denotes the sample observation value; $\hat{y}_i$ is the model prediction value; $\overline{y}$ represents the average value of sample observations.

Table 3 Residual analysis.

Specimen type	Load type	RSS	TSS	R^2
Hollow ring	Loading curve	5.697×10^3	6.202×10^3	0.908
	Unloading curve	3.758×10^3	3.074×10^4	0.878
Solid cylinder	Loading curve	9.874×10^3	5.313×10^5	0.981
	Unloading curve	2.338×10^4	3.682×10^5	0.937

Table 4 Energy error analysis.

Specimen type	Model calculation (J)	Experiment (J)	Relative error (%)
Hollow ring	3.854×10^{-2}	4.179×10^{-2}	8.43
Solid cylinder	1.754×10^{-2}	2.031×10^{-2}	13.64

As indicated in Tables 3 and 4, the residual values R^2 of the FMP-MR hollow ring and solid cylinder are close to 1, and the relative error of energy was small. This effectively demonstrates that the model agreed well with the experimental results.

As indicated in Fig. 17, three cumulative energy consumption growth stages were observed in the FMP-MR displacement energy consumption curve, regardless of the shape and size. However, the numerical value was also different from the duration of each stage owing to the preparation parameters, geometric morphology, and meso-wire turn structure. The segmentation phenomenon of the energy consumption growth curve can be divided into three parts: I guidance phase, II main growth, and III relaxation stages.

In the initial stage of loading (Stage I), large numbers of spatial micropore physical structures existed in the FMP-MR owing to the preparation process characteristics. Hence, the material mainly depended on the self-shrinkage phenomenon between the voids to meet the mutual movement process between the wire turns. Therefore, a small dry friction slip phenomenon existed at the effective contact point in the FMP-MR during the induction stage. Consequently, the displacement energy consumption curve reflected the phased trend of low energy consumption and became the "guiding stage". Moreover, central holes were formed in the annular FMP-MR when compared to the solid cylindrical materials. In addition to the wire turning towards the pore filling direction, the wires also moved inward to the hollow area, resulting in a certain degree of internal expansion effect. During this process, the majority corresponded to the spatial movement of the wire turns, and the contact dry friction phenomenon occurred later with a relatively long guiding stage.

Under an applied load (Stage II), the internal space pores of the FMP-MR were further compressed, and the movable "free volume" (or porosity) of the wire turns was gradually reduced. Therefore, the contact dry friction between the wire turns indicated a significant growth trend (Fig. 17). At this time, FMP-MR energy consumption curves with different shapes revealed a sharp rising stage with varying degrees, becoming the main growth stage. This mainly

depended on the dry friction heat loss mechanism between the wire turns. The main growth stage consisted of the core stage for FMP-MR to complete the functions of damping, energy dissipation, and vibration reduction.

In the relaxation stages (Stage III), the internal porosity of the FMP-MR reached a low level. Under further applied load, it became difficult for global or relative movement in space owing to the sharp reduction in "free volume" between the wire turns coupled with the deterioration of the boundary conditions, such as physical constraints. This indicated the contact state of the stick extrusion of the wire turns. In this state, the number of FMP-MR contact dry frictions decreased significantly. In addition, the macro phenomenon revealed energy growth in the displacement energy consumption curve with a slow or even zero increase stage, which became the "relaxation stage". Note that the "relaxation stage" consisted of a low strain stage in the process of continuous increase in stress, similar to the quasi-creep phenomenon of metal materials under a short time and large load. The size of this stage would significantly influence the lifetime of the FMP-MR. Future work will focus on exploring the mapping relationship between the lifetime and meso-energy consumption mechanism.

In summary, this work not only explored the damping hysteresis mechanism of FMP-MR dry friction but also confirmed the energy evolution process based on the research content and structural characteristics of the wire turn dry friction of the materials. The proposed periodic growth trend of the energy effectively provided a certain degree of guidance for the lifetime prediction of the FMP-MR during production preparation and industrial applications.

5 Conclusions

An FMP-MR spatial finite element model with multipoint random contact characteristics was successfully constructed. A cell group model with an energy dissipation mechanism was proposed to dynamically reconstruct the FMP-MR internal wire turn law, quantitatively discuss the damping energy dissipation characteristics of the material from the perspective of dry friction energy dissipation, and provide the acceptable theoretical guidance for the lifetime prediction of the material. The following conclusions can be drawn.

1) A cell group model with an energy dissipation mechanism was proposed based on the FMP-MR microporous wire turn winding finite element model. The complex spiral network structure of FMP-MR multipoint random contact was accurately reconstructed, and its contact characteristics were tracked in real time in both space and time dimensions based on the characteristics of the space vector.

2) The concept of the effective contact point of FMP-MR was established, and the unique displacement ablation mechanism in meso-scale and quasi-Gaussian distribution of internal meso-contact behavior was obtained to explain the unique characteristics of the highly viscoelastic FMP-MR structure. Using the equivalent friction damping force, an FMP-MR dry friction hysteresis model based on the energy dissipation mechanism was established, and the highly nonlinear damping energy dissipation characteristics of FMP-MR materials were effectively expounded from a multiscale perspective.

3) The study of phased energy loss suggested the lagging of the phased peak of the energy dissipation behind the peak of effective contact points. This indicated that the FMP-MR energy dissipation was jointly determined by the effective contact point and micro-displacement of dry friction inside the material. Moreover, an in-depth discussion of the energy consumption mechanism of FMP-MR was conducted. The results demonstrated three-phased growth laws with different action mechanisms in the guiding, main growth, and relaxation stages of the energy consumption displacement curve owing to the different behavior of the meso-structure during the FMP-MR loading process. This provides an acceptable theoretical basis for the damping energy dissipation mechanism and lifetime prediction of FMP-MR.

Acknowledgements

We thank the National Natural Science Foundation of China (Grant Nos. 52175162, 51805086, and 51975123), the Natural Science Foundation of Fujian Province (Grant No. 2019J01210), and Health education joint project of Fujian Province (Grant No. 2019-WJ-01).

References

[1] Kou H N, Liu G Q, Yang J C, Bai H B. Microstructure and mechanical properties of stainless steel wires used for metal rubber. *J Aero Mater* **26**(4): 24–28 (2006) (in Chinese)

[2] Lu C Z, Li J Y, Zhou B Y. Effect of wire properties on fatigue properties of metal rubber. *Journal of Vibration and shock* **37**(24): 154–159 (2018) (in Chinese)

[3] Zhang W, Xue X, Bai H B. Mechanical and electrical properties of Cu–steel bimetallic porous composite with a double-helix entangled structure. *Compos Struct* **255**: 112886 (2021)

[4] Ma Y H, Zhang Q C, Zhang D Y, Scarpa F, Liu B L, Hong J. The mechanics of shape memory alloy metal rubber. *Acta Mater* **96**: 89–100 (2015)

[5] Ma Y H, Zhang Q C, Zhang D Y, Scarpa F, Liu B L, Hong J. A novel smart rotor support with shape memory alloy metal rubber for high temperatures and variable amplitude vibrations. *Smart Mater Struct* **23**(12): 125016 (2014)

[6] Ma Y H, Tong X L, Zhu B, Zhang D Y, Hong J. Theoretical and experimental investigation on thermophysical properties of metal rubber. *Acta Phys Sinica* **62**(4): 048101 (2013) (in Chinese)

[7] Li T, Bai H B. Compressive property of knitted–dapped metal rubber at different temperatures. *Mater Mech Eng* **42**(10): 58–61 (2018) (in Chinese)

[8] Li Z C, Zhao Y G B, Wang X R, Guo D X, Wang J Y, Zhu L Y. Experimental study on compression and high temperature performance of metallic rubber. *Shanxi Archit* **44**(2): 113–114 (2018) (in Chinese)

[9] Liu Z, Chen H, Wang G S, Lai L Y. Analysis of shock response accelerations of metal-net rubber vibration isolators. *Noise and Vibration Control* **38**(2): 208–211 (2018) (in Chinese)

[10] Wang S C, Deng Z Q. Impact performance test of damping materials for lunar lander. *Missile and Space Launch Technology* (1): 53–56 (2007) (in Chinese)

[11] Cao X B, Wei C, Liang J Q, Wang L X. Design and dynamic analysis of metal rubber isolators between satellite and carrier rocket system. *Mech Sci* **10**(1): 71–78 (2019)

[12] Xiao K, Bai H B, Xue X, Wu Y W. Energy dissipation characteristics and parameter identification of metal rubber coated pipe in high temperature environment. *Ord Mater Sci Eng* **42**(01): 11–17 (2019) (in Chinese)

[13] Zhao C. Design and mechanical properties of metal rubber pipeline shock absorber. Master Thesis. Harbin (China): Harbin Engineering University, 2018.

[14] Jiang F, Ding Z Y, Wu Y W, Bai H B, Shao Y C, Zi B. Energy dissipation characteristics and parameter identification of symmetrically coated damping structure of pipelines under different temperature environment. *Symmetry* **12**(8): 1283 (2020)

[15] Bai C Y, Wei W B, Dang X Q, Wang K Z. Cervical stability changes following metal rubber cervical disc replacement. *Chinese Tissue Engineering Research* **19**(16): 2467–2472 (2015) (in Chinese)

[16] Ao H R, Jiang H Y, Xia Y H, Ulanov A M. Simplified description method of elasto-hysteresis loop of metal rubber material. *Journal of China University of Mining and Technology* **33**(4): 453–456 (2004) (in Chinese)

[17] Li Y Y, Wang W. Generation mechanism and mechanical model of dry friction damping of metal rubber materials. *Machinery Manufacturing and Automation* **43**(6): 158–160 (2014) (in Chinese)

[18] Wu R P, Bai H B, Lu C H. Study on influencing factors and meso model of compression properties of metal rubber. *Sci Technol Eng* **18**(2): 66–71 (2018) (in Chinese)

[19] Zou L Q, Cao Y W, Fu H L, Wang Y. Study on the mechanical model for hysteresis characteristics analysis of metal rubber materials. *Noise and Vibration Control* **39**(6): 1–5, 199 (2019) (in Chinese)

[20] Cao F L, Bai H B, Li D W, Ren G Q, Li G Z. A constitutive model of metal rubber for hysteresis characteristics based on a meso-mechanical method. *Rare Met Mater Eng* **45**(1): 1–6 (2016) (in Chinese)

[21] Cao F L, Bai H B, Li D W, Lu C H, Li G Z. Research on mechanical model of metal rubber for hysteresis characteristic in the non-forming direction. *J Mech Eng* **51**(2): 84–89 (2015) (in Chinese)

[22] Liu W, Wang S, Zhang Z, Xu Y Q, Wang Q. Analysis of dynamic mechanical characteristics of metal rubber damping pad. *Mech Res* **4**: 238–248 (2019) (in Chinese)
[23] Hou J F, Bai H B, Li D W. Damping capacity measurement of elastic porous wire-mesh material in wide temperature range. *J Mater Process Technol* **206**(1–3): 412–418 (2008)
[24] Gadot B, Martinez O R, Roscoat S R D, Bouvard D, Rodney D, Orgéas L. Entangled single-wire NiTi material: A porous metal with tunable superelastic and shape memory properties. *Acta Mater* **96**: 311–323 (2015)
[25] Ertas B, Luo H G, Hallman D. Dynamic characteristics of shape memory alloy metal mesh dampers. In: Proceedings of the 50th AIAA/ASME/ASCE/AHS/ASC Structures, Structural Dynamics, and Materials Conference, Palm Springs, USA, 2012.
[26] Zhu M L, Long J, Xuan F Z. Fatigue life and mechanistic modeling of interior micro-defect induced cracking in high cycle and very high cycle regimes. *Acta Materialia* **157**: 259–275 (2018).
[27] Ren Z Y, Shen L L, Huang Z W, Bai H B, Shen D, Shao Y C. Study on multi-point random contact characteristics of metal rubber spiral mesh structure. *IEEE Access* **7**: 132694–132710 (2019)
[28] Budynas G B. *Advanced Material Mechanics and Practical Stress Analysis*. Beijing (China): Tsinghua University Press, 2001.
[29] Zhang Y H, Liu H H, Wang D C. *Spring Manual*. Beijing (China): China Machine Press, 2008 (in Chinese)
[30] Ren Z Y, Shen L L, Bai H B, Pan L, Zhong S C. Constitutive model of disordered grid interpenetrating structure of flexible microporous metal rubber. *Mech Syst Signal Process* **154**: 107567 (2021)
[31] Ma Y H, Zhang Q C, Wang Y F, Hong J, Scarpa F. Topology and mechanics of metal rubber via X-ray tomography. *Mater Des* **181**: 108067 (2019)
[32] Li L S. Differential geometry of hypersurfaces in N-dimensional Euclidean space. Master Thesis. Wuhan (China): Central China Normal University, 2007.

Liangliang SHEN. He received his B.S. and M.S. degrees from Chongqing University of Technology and Fuzhou University, China, in 2018 and 2021, respectively. His research interests include friction, vibration and noise reduction, and micro mechanism of polymer materials.

Zhiying REN. She received her Ph.D. degree from Fuzhou University, China, in 2015. She is presently a professor and doctoral supervisor of the School of Mechanical Engineering and Automation, Fuzhou University, China. Her research interests include wear resistance and surface characterization technology of equipment parts and the research of metal rubber materials.

Xu JIAN. He received his Ph.D. in composite materials, University of Leuven, Belgium. He is currently employed as a professor in the School of Chemical Engineering, Dalian University of Technology, China. From October 2011 to September 2014, he worked as a research scientist in CommScope, Germany. From September 2014 to November 2016, he worked as a research scientist at the Institute of Advanced Materials in Madrid, Spain. His research interests include the fiber surface modification and development of special equipment for composite materials.

Ling PAN. She received her Ph.D. degree from Fuzhou University, China, in 2015. She is presently a professor and master supervisor of the School of Mechanical Engineering and Automation, Fuzhou University, China. A senior member of the Chinese Mechanical Engineering Society and the director of the Fuzhou Friction and Lubrication Industry Technology Innovation Center. Her main research interests are tribology and mechanical design/theory.

Youxi LIN. He received his Ph.D. degree from Fuzhou University, China, in 2007. He is a director of the Tribological Branch of the Chinese Mechanical Engineering Society. He is now a professor in the School of Mechanical Engineering and Automation and the director of the Mechanical and Electrical Engineering Practice Center, Fuzhou University, China. His research interests include the advanced manufacturing technology and the related tribology research.

Hongbai BAI. He received his Ph.D. degree from Xi'an Jiaotong University, China. He is a professor and doctoral supervisor at Fuzhou University, China. He is the director of Engineering Research Center for Metal Rubber, Fuzhou University, China. His research interests include: non-linear vibration, automotive acoustic fault diagnosis technology, and the research of metal rubber materials.